Power Flow Analysis and Current Optimization Control in Automatic Neutral Section Power Supplier With Partial Capacity

Zhibo Zhang, *Graduate Student Member, IEEE*, Kai Li, *Senior Member, IEEE*,
Changyu Gao, *Graduate Student Member, IEEE*, and Trillion Q. Zheng, *Senior Member, IEEE*

***Abstract*—Addressing the power interruption and speed loss issues induced by the neutral section in electrified railways, numerous automatic neutral section power supplier (ANSPS) systems were proposed. Among these, an ANSPS serving as railway power conditioner on time-division basis stands out for its low converter capacity, high utilization, and multifunctionality. Nevertheless, the current scheme has two points to be improved: one is the unclear power flow caused by circuit coupling, and the other is the excessive difference of current amplitudes and transmission powers in input legs due to the existing current control method, resulting in unbalanced leg heating and aging. To solve these issues, this article analyzes the power calculation method, elaborates on the proportion and path of the transmission power. Then, based on the power flow analysis, a novel current optimization control method is proposed. This method enables equal current amplitudes and balanced power transmission in the input legs, which is more conducive to converter design. In addition, the maximum current and the required capacity of the input bridge legs will also be reduced theoretically. Finally, its effectiveness is validated by the simulation results through MATLAB/Simulink and experimental results of a scaled-down prototype.**

***Index Terms*—Automatic neutral section power supplier, current optimization control method, electrified railway, power flow analysis.**

I. INTRODUCTION

IN high-speed and heavy-haul railways, the single-phase line frequency ac traction power supply is a commonly adopted approach [1]. As a single-phase load, electric locomotives induce negative sequence currents in the three-phase public power grid, thus affecting the stable operation of the grid [2].

To mitigate negative sequence currents, the traction power supply system adopts the phase-shifting power supply mode [3], as depicted in Fig. 1(a). Specifically, by changing the connection method of the traction transformer, the voltage phases of adjacent feeding sections are altered sequentially [4]. To prevent phase-to-phase short circuits, a neutral section is set up for isolation [5]. Before a train approaches the neutral section, it is customary to open the on-board main circuit breaker. Then, the train coasts through the neutral section by inertia [6]. After the train leaves the neutral section, the on-board main circuit breaker is closed again. However, this procedure leads to speed loss of the train, and in cases of insufficient speed, the train might even halt within the neutral section [7]. Moreover, when the pantograph of the train is passing the transition area, overvoltages and arcs are likely to occur [8]. Collectively, these issues endanger the operational safety and normal running order of the train.

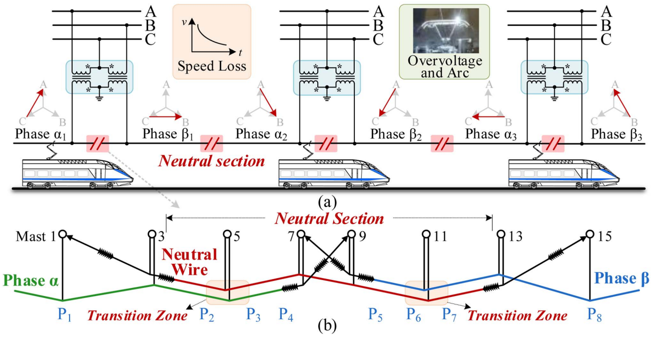

Fig. 1. Structure of traction power supply system for AC electrified railway. (a) Traction power supply system with phase rotation connection. (b) Structure of a seven-cross neutral section with overlaps.

To address these issues, researchers have adopted two approaches. One involves a comprehensive transformation of the traction power supply system, such as flexible traction power supply [9], [10] or cophase power supply [11], [12]. The other focuses on conducting partial modifications to the existing traction power supply system to enable power supply to the neutral section, exemplified by the automatic neutral section power supplier (ANSPS) system based on switches [13], [14] and the ANSPS system based on voltage source converters (VSC) [15], [16]. Among these methods, the ANSPS system based on VSC can eliminate overvoltages and power supply dead zones, achieving an effect comparable to that of the first approach [17] (i.e., the comprehensive transformation of the traction power supply system), while significantly reducing costs. Hence, it has been studied by many scholars as a promising technical route. The ANSPS scheme based on back-to-back converters

Received 13 March 2025; revised 4 June 2025; accepted 15 July 2025. Date of publication 18 July 2025; date of current version 8 September 2025. This work was supported by the National Natural Science Foundation of China under Grant 52477173. Recommended for publication by Associate Editor C. Rojas. *(Corresponding author: Kai Li.)*

The authors are with the School of Electrical Engineering, Beijing Jiaotong University, Beijing 100044, China (e-mail: zbzhang@bjtu.edu.cn; kaili@bjtu.edu.cn; changyugao@bjtu.edu.cn; tqzheng@bjtu.edu.cn).

Color versions of one or more figures in this article are available at https://doi.org/10.1109/TPEL.2025.3590634.

Digital Object Identifier 10.1109/TPEL.2025.3590634

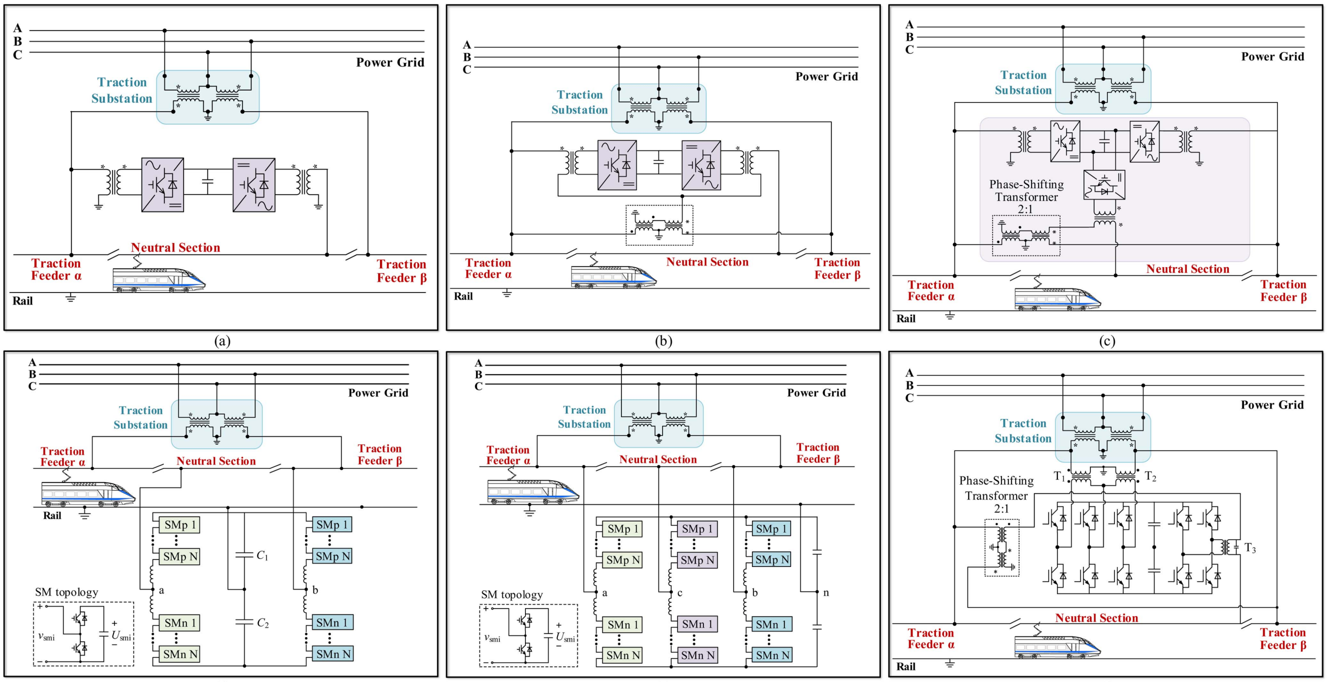

(a) (b) (c) (d) (e) (f)

Fig. 2. Structure of existing ANSPS schemes. (a) Back-to-back converter structure. (b) Back-to-back converter structure with phase-shifting transformer. (c) Back-to-back converter structure with an additional common DC bus inverter. (d) Two-phase modular multilevel converter structure (MMC). (e) Three-phase MMC structure. (f) Three-phase converter input with single-phase H-bridge output.

was proposed in the early stage [18], [19]. In this scheme, the rectifier side and the inverter side of the converter are decoupled via the dc side, facilitating independent design of the two-stage converters. Moreover, it allows for the smooth switching of the neutral section voltage from one phase feeding section voltage to another. Subsequently, the ANSPS system based on the three-leg converter was proposed [20]. Thanks to the dc midpoint grounding in this scheme, each leg can be independently controlled, and the control of the neutral section voltage can also be realized. In all of the above schemes, all the power of the electric locomotive derives from the power processed by the converters, which can be regarded as a full-power converter scheme. Given the relatively high traction power of electric locomotives, the required converters entail higher costs.

To reduce the cost of the converter, a phase-shifting transformer formed by two transformers connected in series is added to the inverter side of ANSPS system to share a portion of the power and cut down the capacity of the converter [21]. In [22], an extra inverter and a phase-shifting transformer are added to the dc bus of back-to-back converters for power supply to the neutral section, and the required converter power is also decreased. By adding additional converters and phase-shifting transformers, the ANSPS scheme based on [22] can be applied in double-track railways [23]. In [24], the ANSPS is constructed based on a three-leg converter, and the converter capacity is also reduced by adding a phase-shifting transformer. This scheme not only can realize the uninterrupted power supply to the neutral section, but also has the functions of railway power conditioner (RPC). Evidently, adding a phase-shifting transformer is a common approach to reducing the converter's capacity within the ANSPS system. Through power sharing by the transformer, a partial power processing converter is, thus, formed. However, due to the addition of multiple large-capacity transformers, the overall volume and footprint of the system become relatively large. Moreover, the cost advantage resulting from the reduction in converter capacity is not significant because of the costs associated with the additional transformers.

In [25], we proposed a novel ANSPS scheme, which can achieve a similar effect as using a phase-shifting transformer in terms of converter's capacity, but without the necessity of adding extra transformers. By comparing the running time of the train on the whole line, it is found that the time of the train in the neutral section is extremely short [26]. Specifically, in over 95% of the time, no train passes through the neutral section, resulting in the converters in other schemes being idle for long periods. In this scheme, when no train passes through the neutral section, the converter serves as an RPC for power quality management, thus improving the utilization rate of the device. Six typical existing ANSPS topologies are shown in Fig. 2, and their comprehensive theoretical performance comparisons are listed in Table I. Although the scheme of this article has certain advantages, due to its special circuit structure, there are some problems, enumerated as follows.

1) In the circuit, due to the coupling between the voltages and currents on the input and output sides, the power flow of the system remains ambiguous. Moreover, a detailed power analysis is lacking, the proportions and distributions of the direct transmission power and the converter processing power are also unknown, thereby hindering the optimization of the current control algorithm.

TABLE I
COMPREHENSIVE THEORETICAL PERFORMANCE COMPARISON OF EXISTING ANSPS

Schemes	Ref	Uninterrupted power supply in neutral section	Power quality management function	Required converter capacity	Device Utilization
Fig.2 (a)	[18]	√	×	+++	++
Fig.2 (b)	[21]	√	×	+	++
Fig.2 (c)	[22]	√	√	++++	+++
Fig.2 (d)	[17]	√	×	+++	++
Fig.2 (e)	[20]	√	√	+++++	+++
Fig.2 (f)	[24]	√	√	++++	+++
This article	[25]	√	√	++	++++

Note: The number of plus signs (+) denotes relative magnitude, not absolute quantitative values. The more plus signs, the greater the required converter capacity or device utilization rate.

2) The present current control method may lead to a significant difference in the current amplitudes of the two legs. This difference might cause variations in the heating and aging rates of the two legs, which is unfavorable for the balanced design of the converter.

This article is a continuation of the research presented in [25]. In response to these two issues, this article conducts power analysis and proposes a novel current optimization control method while ensuring that the ANSPS system provides uninterrupted power supply for trains passing through the neutral section without overvoltage and arcing. The main contributions of this article are summarized as follows.

1) The power flow within the system is analyzed, and the power calculation method is elaborated. Subsequently, the variations of the terminal transmission power, the converter processing power and the direct transmission power in each phase with respect to the phase shift angle are computed. The limitations of the original current control strategy are identified from a power perspective, which lays the foundation for the proposed decoupled current optimization control.
2) A current optimization decoupling control method is proposed, which enables a more balanced current amplitude in the input legs. This prompts the redistribution of the direct transmission power among the input legs, which results in more balanced power transmission at each port and facilitates converter design.

The rest of this article is organized as follows. In Section II, the configuration and working process of the ANSPS system are introduced, and the principle and effect of existing current control method are analyzed. In Section III, the power flow within the system is analyzed, and the power calculation method is elaborated. Subsequently, the variations of the converter processing power and the direct transmission power in each phase with respect to the phase shift angle are computed. In Section IV, a current optimization control method is proposed, which enables a more balanced current amplitude and power. In Sections V and VI, the effectiveness and superiority of the current optimization control strategy of ANSPS are validated through the simulation and the experimental results of a laboratory low-power prototype. Finally, Section VII concludes this article.

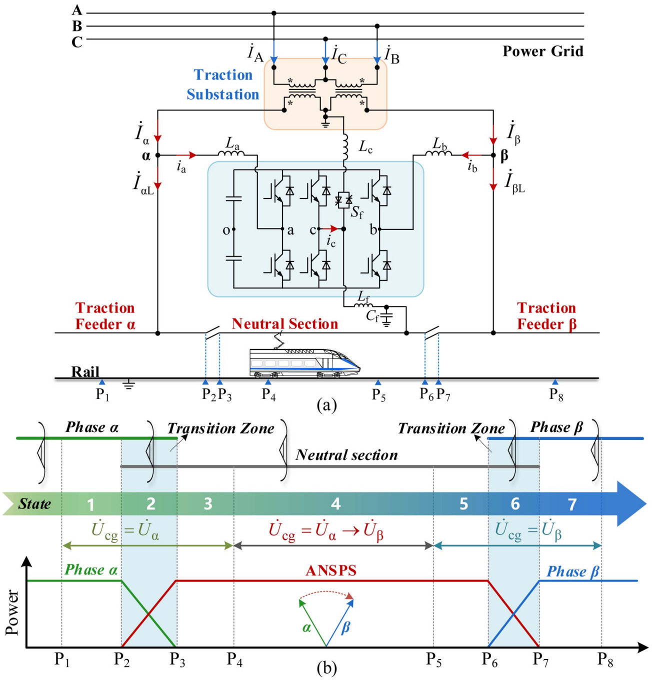

Fig. 3. Configuration and working process of the system. (a) Configuration of the ANSPS system as proposed in [25]. (b) Whole working process of the system.

II. SYSTEM CONFIGURATION AND EXISTING CURRENT CONTROL ANALYSIS

In this section, the structure and working principle of the ANSPS system are introduced. By analyzing the issue of coupling between the voltages and currents on the input side and the output side, a concise introduction to the existing current decoupling control method is provided, and the results derived from this method is demonstrated. Meanwhile, the symmetrical characteristic in this current decoupling algorithm is pointed out, which lays a foundation for analyzing the power characteristics.

A. System Configuration and Working Process

The configuration of the ANSPS system proposed in [25] is depicted in Fig. 3(a). In this article, the traction substation

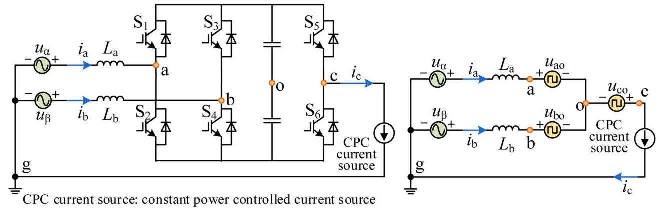

CPC current source: constant power controlled current source

Fig. 4. Circuit diagram and equivalent model.

adopts V/v traction transformers. The phase difference of the voltages between two adjacent feeding sections is $\pi/3$. Given the relatively high voltage level of the catenary, in practical engineering applications, it is requisite for the converter to adopt a multilevel topology. For the purpose of facilitating the description in this article, a two-level converter is utilized to simplify the representative circuit without compromising the fundamental circuit principle. To enhance the utilization rate of the converter, it is configured to operate as an RPC when no train is passing through the neutral section. The switch S_f, also referred to as the function selector, can be realized by using a series of thyristor valve groups or a high-voltage circuit breaker. The circuit structure is modified by the operation of the function selector switch S_f, thereby achieving the time-division multiplexing of the converter.

Ignoring the impedance of the wires in the system, the equivalent circuit diagram of the system in ANSPS mode is depicted in the Fig. 4. u_α and u_β represent the voltage of feeding section α and β. The external port characteristics of electric locomotives can be regarded as a current source under constant power control within a certain time scale. Each phase leg of the converter is equivalent to a controlled voltage source, and the output voltages of each phase leg are u_ao, u_bo, and u_co, where o is dc virtual midpoint. u_ag, u_bg, u_cg, and u_og represent the potentials of points a, b, c, and o, where g is regarded as the potential reference zero.

The operation of the system strongly depends on accurate train position detection, particularly the pantograph's location. As shown in Fig. 3(a), position detection sensors, such as LiDAR, are installed at points P_1–P_8 to detect the pantograph location of the train. When the train is located outside the neutral section, specifically before point P_1 or after point P_8, the switch S_f remains closed, and the system functions in RPC mode for power quality management. In this mode, conventional control strategies, as detailed in [25], are employed and will not be discussed further herein.

As the train enters the neutral section (from point P_1 to point P_8, assuming movement from left to right), the switch S_f is turned OFF, and the control process is divided into seven operational states, as illustrated in Fig. 3(b).

State 1: The ANSPS system performs no-load inversion, with the converter output voltage u_cg tracking that of feeding section α u_α. This prevents arcing caused by voltage inequality between the feeding section α and the neutral section as the pantograph enters the transition zone.

State 2: When the system is in State 2, the pantograph simultaneously overlaps the feeding section α and the neutral section. At this stage, the ANSPS system operates in a transitional state, during which the power from feeding section α is gradually transferred to the converter. This power transfer must be fully completed before the pantograph reaches point P_3.

State 3: The converter maintains its output voltage u_cg equal to that of feeding section α u_α.

State 4: The phase shifting of the output voltage u_cg is carried out, gradually transitioning the output voltage from phase α to phase β.

State 5 to 7: The subsequent States 5, 6, and 7 represent the process of the train exiting the neutral section, which can be, respectively, regarded as the symmetrical processes of States 3, 2, and 1. For brevity, detailed descriptions are omitted.

When the system is in States 2–6, the existing current decoupling control method may lead to a significant difference in the amplitude of the two input currents. This indicates that there is still ample room for optimization. To achieve optimization, a further analysis of the circuit will be carried out first.

B. Circuit Analysis

All the output current i_c of the converter comes from the input currents i_a and i_b. Thus, within one cycle, the sum of the input-side currents is equal to the output current, which means that

$$\dot{I}_\mathrm{a} + \dot{I}_\mathrm{b} = \dot{I}_\mathrm{c} \tag{1}$$

where $\dot{I}_\mathrm{a}$, $\dot{I}_\mathrm{b}$, and $\dot{I}_\mathrm{c}$ represent the phase currents of the converter, regarding the voltage of feeding section $\dot{U}_\alpha$ to be the phase angle reference zero. It can be seen from (1) that there is a coupling relationship between the input current and the output current.

Point o may not necessarily exist in the circuit, its potential is a virtual, floating potential. The system output voltage u_cg can be considered as the superposition of the output voltage of the c-phase leg u_co and the potential of the dc virtual midpoint u_og

$$u_\mathrm{cg} = u_\mathrm{co} + u_\mathrm{og}. \tag{2}$$

According to KVL, the relationships between the potential of the dc virtual midpoint u_og and the input bridge leg are

$$u_\alpha - L_\mathrm{a}\frac{\mathrm{d}i_\mathrm{a}}{\mathrm{d}t} - u_\mathrm{ao} = u_\mathrm{og} \tag{3}$$

$$u_\beta - L_\mathrm{b}\frac{\mathrm{d}i_\mathrm{b}}{\mathrm{d}t} - u_\mathrm{bo} = u_\mathrm{og}. \tag{4}$$

It can be seen from (2), (3), and (4) that the potential of the dc virtual midpoint u_og is affected by the three-phase bridge leg of the converter. Therefore, the selection of the reference value of the midpoint potential will also affect the amplitude of the converter leg voltage u_ao, u_bo, and u_co.

When analyzing the selection of reference value of the midpoint potential, the voltage on the inductor is ignored because the voltage on the inductor is quite small relative to the voltage of feeding section. The phasor diagram of the system in ANSPS mode is shown in Fig. 5. The reference value of the dc virtual midpoint potential $\dot{U}_\mathrm{og}$ is selected as the midpoint of the phasor difference between the voltages of the two feeding sections $\dot{U}_\alpha$ and $\dot{U}_\beta$. The output voltage amplitudes of $\dot{U}_\mathrm{ao}$, $\dot{U}_\mathrm{bo}$, $\dot{U}_\mathrm{co}$ are equal and reach their minimum. Therefore, this point is an ideal virtual midpoint potential reference value in this mode, which

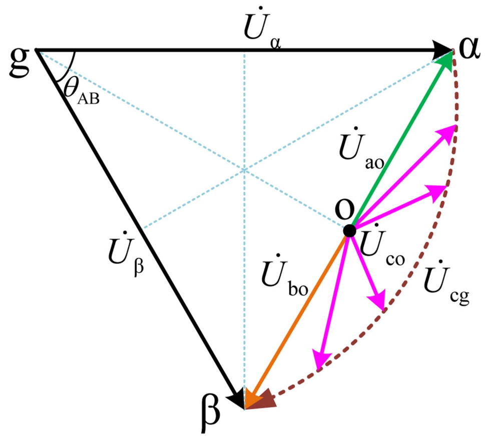

Fig. 5. Phasor diagram of the system in ANSPS mode when DC virtual midpoint potential is at the middle point of the voltage difference between feeding sections.

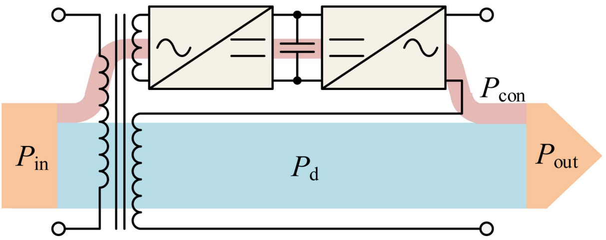

Fig. 6. Power diagram of a typical hybrid transformer.

can be expressed as

$$\dot{U}_{\mathrm{og}}=\frac{1}{2}\left(\dot{U}_{\alpha}+\dot{U}_{\beta}\right). \tag{5}$$

A converter in which only a portion of the power is processed by the converter and the remaining part is directly transmitted to the load without being processed by the converter is referred to as a partial power processing converter [28]. Fig. 6 illustrates a typical hybrid transformer topology where the converter and the transformer are connected in series to supply power to the load [27]. In this topology, the power transmitted by the transformer, denoted as P_{d}, is defined as the direct transmission power, while the power processed by the converter and then supplied to the load is defined as the converter processing power, denoted as P_{con}. The converter in this article is a partial power processing converter, where a portion of the power can be directly transferred from the input side to the output side, and a detailed analysis will be conducted in Section III.

C. Existing Principle of Current Decoupling Control

When the locomotive is located in the neutral section, the system needs to control the output voltage $\dot{U}_{\mathrm{cg}}$ of the converter so that the voltage in the neutral section can smoothly complete the phase shift. The current $\dot{I}_{\mathrm{c}}$ is determined by the traction power of the locomotive. During this process, it is essential to maintain the balance between the input and output powers while adhering to the current relationship of (1). This calls for the design of a current decoupling control to reasonably allocate the load current of the locomotive to the input-side legs, thereby maintaining the constant dc voltage of the converter. When the locomotive is located in the transition zone, taking Stage 2 as an example, since the pantograph simultaneously overlaps the neutral section and the feeding section α, the output voltage $\dot{U}_{\mathrm{cg}}$ of the ANSPS system is clamped to $\dot{U}_{\alpha}$ as well. At this moment, introduce the target value of the output current into the current decoupling control, so as to obtain the target value of the current of the input-side bridge legs. In this way, the transfer of the output power of the converter can be achieved as expected.

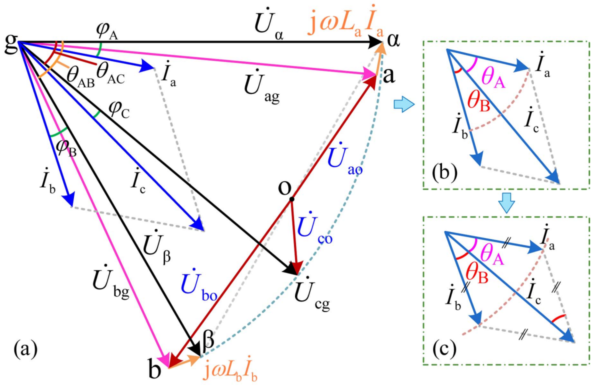

Fig. 7. Phasor diagram of input and output currents and voltages. (a) Phase angle relationships between voltages and currents. (b) Phase angles between the currents when the input current amplitudes are not equal. (c) Phase angles between the currents when the input current amplitudes are equal.

As analyzed above, the current decoupling algorithm is supposed to reasonably allocate the load current $\dot{I}_{\mathrm{c}}$ to the input-side bridge legs and take it as their current reference values under the circumstances of satisfying the balance of active power between the input and output as well as the current coupling relationship. The phasor diagram of the system's voltage and current is shown in Fig. 7.

Based on the balance of active power, (6) is formulated

$$U_{\alpha}I_{\mathrm{a}}\cos\varphi_{\mathrm{A}}+U_{\beta}I_{\mathrm{b}}\cos\varphi_{\mathrm{B}}=U_{\mathrm{cg}}I_{\mathrm{c}}\cos\varphi_{\mathrm{C}}. \tag{6}$$

The angle between $\dot{I}_{\mathrm{a}}$ and $\dot{I}_{\mathrm{c}}$ is denoted as θ_{A}. The angle between $\dot{I}_{\mathrm{b}}$ and $\dot{I}_{\mathrm{c}}$ is denoted as θ_{B}, as shown in Fig. 7(b). The load current $\dot{I}_{\mathrm{c}}$ and catenary voltage in neutral section $\dot{U}_{\mathrm{cg}}$ are measured, and $\dot{U}_{\alpha}$ and $\dot{U}_{\beta}$ are also measured. The angle between $\dot{U}_{\alpha}$ and $\dot{U}_{\beta}$ is θ_{AB}. The angle between the output voltage $\dot{U}_{\mathrm{cg}}$ and the voltage of α-phase feeding section $\dot{U}_{\alpha}$ is defined as the phase shift angle, which is represented by θ_{AC}, this angle will change accordingly with the position of the train

$$\theta_{\mathrm{A}}=\theta_{\mathrm{AC}}+\varphi_{\mathrm{C}}-\varphi_{\mathrm{A}} \tag{7}$$

$$\theta_{\mathrm{B}}=\theta_{\mathrm{AB}}-\theta_{\mathrm{AC}}-\varphi_{\mathrm{C}}+\varphi_{\mathrm{B}}. \tag{8}$$

According to the coupling relationship between input and output currents in (1), (9), and (10) are derived respectively along the direction of the output current $\dot{I}_{\mathrm{c}}$ and perpendicular to $\dot{I}_{\mathrm{c}}$

$$I_{\mathrm{a}}\cos\theta_{\mathrm{A}}+I_{\mathrm{b}}\cos\theta_{\mathrm{B}}=I_{\mathrm{c}} \tag{9}$$

$$I_{\mathrm{a}}\sin\theta_{\mathrm{A}}-I_{\mathrm{b}}\sin\theta_{\mathrm{B}}=0. \tag{10}$$

In (6)–(10), I_{c}, U_{cg}, φ_{C}, U_{α}, U_{β}, θ_{AC}, and θ_{AB} are known, while I_{a}, I_{b}, θ_{A}, and θ_{B} are unknown, φ_{A} and φ_{B} can be determined by θ_{A} and θ_{B} according to (7) and (8). Based on

(9) and (10), (6) can be transformed into (11) represented by I_a and θ_A

$$I_\mathrm{a}\sin\left(\theta_\mathrm{A}-\varphi_\mathrm{k}\right)=\frac{U_\mathrm{cg}\cos\varphi_\mathrm{C}-U_\beta\cos\left(\theta_\mathrm{AC}+\varphi_\mathrm{C}-\theta_\mathrm{AB}\right)}{\sqrt{k_1^2+k_2^2}}I_\mathrm{c} \tag{11}$$

where three intermediate variables are introduced. This simplification method comes from [25]

$$k_1=U_\alpha\sin\left(\theta_\mathrm{AC}+\varphi_\mathrm{C}\right)-U_\beta\sin\left(\theta_\mathrm{AC}+\varphi_\mathrm{C}-\theta_\mathrm{AB}\right) \tag{12}$$

$$k_2=-U_\alpha\cos\left(\theta_\mathrm{AC}+\varphi_\mathrm{C}\right)+U_\beta\cos\left(\theta_\mathrm{AC}+\varphi_\mathrm{C}-\theta_\mathrm{AB}\right) \tag{13}$$

$$\varphi_\mathrm{k}=\arctan\left(\frac{k_2}{k_1}\right). \tag{14}$$

A simple, feasible, and computationally-efficient calculation method in engineering is provided in [25]. This calculation method aims to maximize the absolute value of the trigonometric function to minimize the current of one phase

$$\left|\sin\left(\theta_\mathrm{A}-\varphi_\mathrm{k}\right)\right|=1. \tag{15}$$

The minimum value of I_a and its corresponding θ_A are obtained. Considering that I_a represents the rms value of a-phase current, $I_\mathrm{a}>0$ is followed. The minimum value of I_a is expressed as follows:

$$I_\mathrm{a}=\frac{\left|U_\mathrm{cg}\cos\varphi_\mathrm{C}-U_\beta\cos\left(\theta_\mathrm{AC}+\varphi_\mathrm{C}-\theta_\mathrm{AB}\right)\right|}{\sqrt{k_1^2+k_2^2}}I_\mathrm{c} \tag{16}$$

$$\theta_\mathrm{A}=\begin{cases}\varphi_\mathrm{k}+\frac{\pi}{2} & \text{when}\quad U_\mathrm{cg}\cos\varphi_\mathrm{C}-U_\beta\cos\left(\theta_\mathrm{AC}+\varphi_\mathrm{C}-\theta_\mathrm{AB}\right)\geq 0\\ \varphi_\mathrm{k}-\frac{\pi}{2} & \text{when}\quad U_\mathrm{cg}\cos\varphi_\mathrm{C}-U_\beta\cos\left(\theta_\mathrm{AC}+\varphi_\mathrm{C}-\theta_\mathrm{AB}\right)<0.\end{cases} \tag{17}$$

By substituting I_a and θ_A into (9) and (10), I_b and θ_B can be obtained. Up to now, the reference values of the input currents $\dot{I}_\mathrm{a}$ and $\dot{I}_\mathrm{b}$ can be calculated. These reference values are a function of the phase shift angle θ_AC.

The aforesaid solution is obtained by minimizing the a-phase current. Depending on different simplification methods, it can also be solved by minimizing the b-phase current, in which case (6) is simplified to

$$I_\mathrm{b}\sin(\theta_\mathrm{B}+\varphi_\mathrm{k})=\frac{U_\mathrm{cg}\cos\varphi_\mathrm{C}-U_\alpha\cos\left(\theta_\mathrm{AC}+\varphi_\mathrm{C}\right)}{\sqrt{k_1^2+k_2^2}}I_\mathrm{c}. \tag{18}$$

It can also maximize the absolute value of the trigonometric function, so that the value of I_b is minimized. Thus, another set of input current reference values $\dot{I}_\mathrm{a}$ and $\dot{I}_\mathrm{b}$ is solved.

D. *Results Analysis of Existing Current Decoupling Control*

The results corresponding to these two solution methods are shown in Figs. 8 and 9, respectively. Fig. 8 shows the results based on the minimum current I_a as the solving condition. Fig. 9 shows the results based on the minimum current I_b as the solving condition. In these two figures, the locomotive load is 9600 kW, the load current is about 350 A, and the power factor is 1. During the phase-shifting process, the input-side bridge leg currents are always smaller than the load current. Based on this, when designing the bridge leg capacity, the load current is used as the current capacity of the input bridge leg.

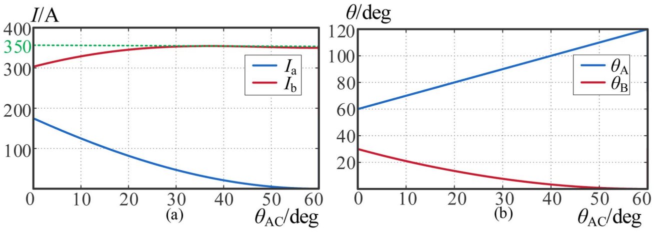

Fig. 8. Reference value of input currents obtained based on the minimum current I_a as the solving condition. (a) Variation of current amplitude with phase shift angle. (b) Variation of current angles with phase shift angle.

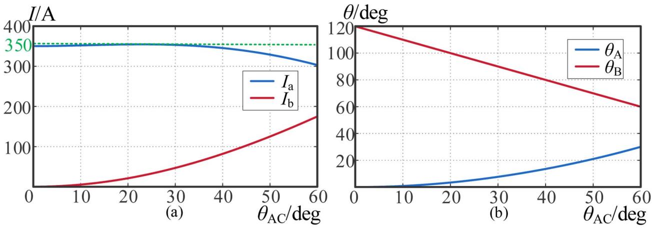

Fig. 9. Reference value of input currents obtained based on the minimum current I_b as the solving condition. (a) Variation of current amplitude with phase shift angle. (b) Variation of current angles with phase shift angle.

Furthermore, it can be observed from Figs. 8 and 9 that there seems to be a certain symmetrical relationship among the results. Through relevant formulas, it can be demonstrated that when the voltages of the traction feeders are equal and the power factor is 1 (in most cases, the voltages and loads of electrified railways approximately meet such conditions), the results obtained by these two methods are symmetrical about $\theta_\mathrm{AC}=30°$. For example, the result obtained by solving with the minimum a-phase current at $\theta_\mathrm{AC}=0°$ is the same as that obtained by solving with the minimum b-phase current at $\theta_\mathrm{AC}=60°$.

Consequently, due to this symmetrical relationship, in the subsequent power analysis, it suffices to conduct the analysis only with the minimum a-phase current instead of considering both. From the perspective of the variation trend of current amplitudes, significant differences can be observed in the amplitudes of the bridge leg currents on the input side, which leads to varying degrees of heat generation among them. This may result in different aging speeds of the bridge legs, thus being unfavorable for the converter design. Moreover, large differences in current amplitudes can also exert adverse effects on the negative sequence current on the grid side. In this article, after conducting power analysis, the current decoupling control will be optimized to make the bridge leg currents more balanced.

III. SYSTEM POWER ANALYSIS

A. *Direct Transmission Power and Converter Processing Power Analysis*

This converter has two input terminals and one output terminal. The entire converter is suspended at a specific potential, which is the dc virtual midpoint potential. For the output voltage u_cg, it is the superposition of the dc virtual midpoint potential u_og

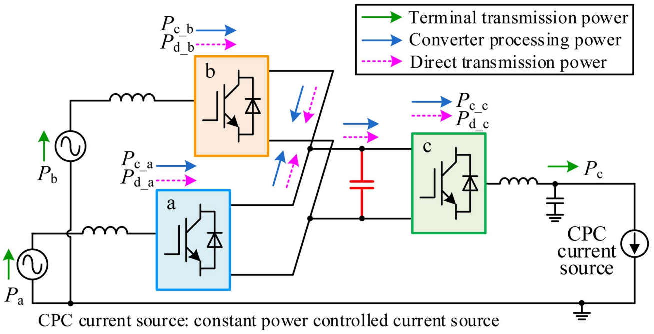

CPC current source: constant power controlled current source

Fig. 10. Schematic diagram of power flow transmission in ANSPS system.

and the output voltage of the c-phase bridge leg u_{co}, and the dc virtual midpoint potential contains a part of the feeding section voltage u_α or u_β. Therefore, the output voltage can be regarded as being composed of part of the feeding section voltages. The output voltage u_{cg} can be expressed as

$$u_{cg} = u_\alpha - L_a \frac{di_a}{dt} - u_{ao} + u_{co} \tag{19}$$

$$u_{cg} = u_\beta - L_b \frac{di_b}{dt} - u_{bo} + u_{co}. \tag{20}$$

Thus, only a part of the power obtained by the load comes from the processing of the converter, while the remaining part comes from the direct transmission power of the power supply. The power flow transmission is depicted in Fig. 10. It should be noted that, unless otherwise specified, the power mentioned here all refers to active power. The power at each terminal consists of two parts: one is the direct transmission power, and the other is the converter processing power. Subsequently, the converter processing active powers P_{c_a}, P_{c_b}, and P_{c_c} of each phase bridge leg will be calculated, respectively, to find the relationship between the terminal transmission active powers P_a, P_b, and P_c and the direct transmission active power P_{d_a}, P_{d_b}, and P_{d_c}.

The complex power transmitted at each terminal is obtained by multiplying the terminal-to-ground voltage by the conjugate of the current. For phase a, the complex power $\dot{S}_a$ is expressed as (21), where the real part represents the active power and the imaginary part corresponds to the reactive power

$$\begin{aligned} \dot{S}_a &= \dot{U}_{ag}\dot{I}_a^* = \left(\dot{U}_\alpha - j\omega L_a \dot{I}_a\right)\dot{I}_a^* \\ &= U_\alpha I_a \cos\varphi_A + j\left(U_\alpha I_a \sin\varphi_A - \omega L_a {I_a}^2\right) \\ &= P_a + jQ_a. \end{aligned} \tag{21}$$

Therefore, the terminal transmission power of the a phase P_a is (22), and the terminal transmission power of the b phase P_b is (23), and the terminal transmission power of c phase P_c is (24). These powers have appeared in (6) in the previous text and are used to calculate power balance

$$P_a = U_\alpha I_a \cos\varphi_A \tag{22}$$

$$P_b = U_\beta I_b \cos\varphi_B \tag{23}$$

$$P_c = U_{cg} I_c \cos\varphi_C. \tag{24}$$

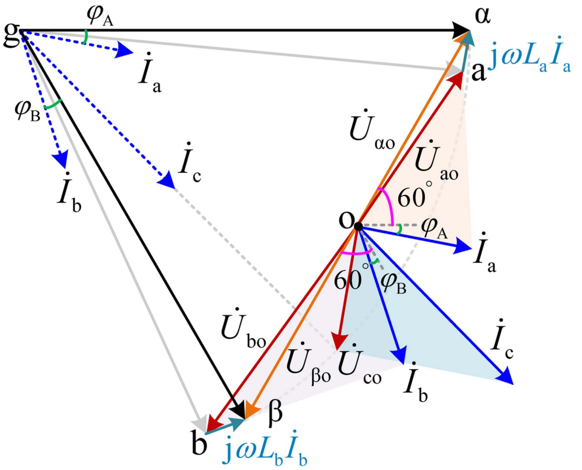

Fig. 11. Phasor diagram of voltages and currents in the bridge legs of converter.

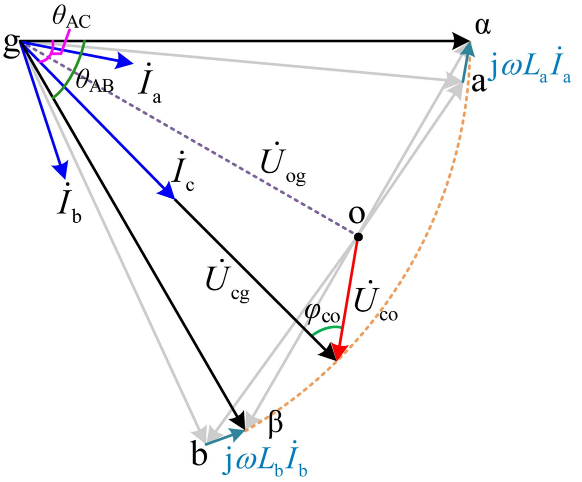

Fig. 12. Phasor diagram of output voltage and current in the converter.

The converter processing power refers to the active power generated by the product of bridge leg output voltage and the bridge leg current. The phasor diagram of voltages and currents in the internal bridge legs of converter is shown in Fig. 11. The phasor diagram of output voltage and current in the converter is shown in Fig. 12.

The complex power of the converter processing of phase a is denoted as $\dot{S}_{c\_a}$, which can be expressed as

$$\begin{aligned} \dot{S}_{c\_a} &= \dot{U}_{ao}\dot{I}_a^* = \left(\dot{U}_{\alpha o} - j\omega L_a \dot{I}_a\right)\dot{I}_a^* \\ &= U_{\alpha o} I_a \cos\left(\varphi_A + 60^\circ\right) \\ &\quad + j\left(U_{\alpha o} I_a \sin\left(\varphi_A + 60^\circ\right) - \omega L_a {I_a}^2\right) \end{aligned} \tag{25}$$

where the real part is the convert processing power P_{c_a} of phase a

$$P_{c\_a} = U_{\alpha o} I_a \cos\left(\varphi_A + 60^\circ\right). \tag{26}$$

Similarly, the complex power of the converter processing of phase a is denoted as $\dot{S}_{c\_b}$, and the converter processing power

$P_{\mathrm{c\_b}}$ of phase b is expressed in (28)

$$\begin{aligned}\dot{S}_{\mathrm{c\_b}} &= \dot{U}_{\mathrm{bo}}\dot{I}_{\mathrm{b}}^{*} = \left(\dot{U}_{\beta\mathrm{o}} - \mathrm{j}\omega L_{\mathrm{b}}\dot{I}_{\mathrm{b}}\right)\dot{I}_{\mathrm{b}}^{*}\\ &= U_{\mathrm{bo}}^{*}I_{\mathrm{b}}\cos\left(60^{\circ}-\varphi_{\mathrm{b}}\right)\\ &\quad + \mathrm{j}\left(U_{\mathrm{bo}}^{*}I_{\mathrm{b}}\sin\left(60^{\circ}-\varphi_{\mathrm{b}}\right) - \omega L_{\mathrm{b}}{I_{\mathrm{b}}}^{2}\right) \qquad (27)\end{aligned}$$

$$P_{\mathrm{c\_b}} = U_{\beta\mathrm{o}}I_{\mathrm{b}}\cos\left(60^{\circ}-\varphi_{\mathrm{B}}\right). \qquad (28)$$

In order to calculate the converter processing power $P_{\mathrm{c\_c}}$, it is necessary to calculate the amplitude of the bridge leg voltage of phase c U_{co} and the angle φ_{co} between the phase current $\dot{I}_{\mathrm{c}}$ and $\dot{U}_{\mathrm{co}}$. The amplitude of U_{co} will change with the phase shift angle θ_{AC}. According to the cosine theorem, U_{co} has such a relationship

$$U_{\mathrm{og}} = U_{\alpha}\cos\left(\frac{\theta_{\mathrm{AB}}}{2}\right) = \frac{\sqrt{3}}{2}U_{\alpha} \qquad (29)$$

$$U_{\mathrm{co}}^{2} = U_{\mathrm{cg}}^{2} + U_{\mathrm{og}}^{2} - 2U_{\mathrm{cg}}U_{\mathrm{og}}\cos\left(\theta_{\mathrm{AC}}-30^{\circ}\right). \qquad (30)$$

After simplification, U_{co} can be expressed as

$$U_{\mathrm{co}} = U_{\alpha}\sqrt{\frac{7}{4} - \sqrt{3}\cos\left(\theta_{\mathrm{AC}}-30^{\circ}\right)}. \qquad (31)$$

When $\theta_{\mathrm{AC}} \geq \frac{\theta_{\mathrm{AB}}}{2} = 30^{\circ}$, based on the sine theorem, φ_{co} has such a relationship

$$\frac{\sin\varphi_{\mathrm{co}}}{U_{\mathrm{og}}} = \frac{\sin\left(\theta_{\mathrm{AC}}-30^{\circ}\right)}{U_{\mathrm{oc}}}. \qquad (32)$$

After simplification, φ_{co} can be expressed as

$$\sin\varphi_{\mathrm{co}} = \frac{\frac{\sqrt{3}}{2}\sin\left(\theta_{\mathrm{AC}}-30^{\circ}\right)}{\sqrt{\frac{7}{4} - \sqrt{3}\cos\left(\theta_{\mathrm{AC}}-30^{\circ}\right)}}. \qquad (33)$$

When $\theta_{\mathrm{AC}} < \frac{\theta_{\mathrm{AB}}}{2} = 30^{\circ}$, φ_{co} has such a relationship (34), so φ_{co} can be expressed as (35)

$$\frac{\sin\varphi_{\mathrm{co}}}{U_{\mathrm{og}}} = \frac{\sin\left(30^{\circ}-\theta_{\mathrm{AC}}\right)}{U_{\mathrm{oc}}} \qquad (34)$$

$$\sin\varphi_{\mathrm{co}} = \frac{\frac{\sqrt{3}}{2}\sin\left(30^{\circ}-\theta_{\mathrm{AC}}\right)}{\sqrt{\frac{7}{4} - \sqrt{3}\cos\left(\theta_{\mathrm{AC}}-30^{\circ}\right)}}. \qquad (35)$$

When the locomotive is in traction state, regardless of whether the sine value of φ_{co} is (33) or (35), the cosine value of φ_{co} can be expressed as

$$\cos\varphi_{\mathrm{co}} = \sqrt{1 - \left(\sin\varphi_{\mathrm{co}}\right)^{2}}. \qquad (36)$$

Based on the abovementioned analysis, the converter processing power of phase c $P_{\mathrm{c{\cdot}c}}$ is expressed as

$$\begin{aligned}P_{\mathrm{c\_c}} &= U_{\mathrm{co}}I_{\mathrm{c}}\cos\varphi_{\mathrm{co}}\\ &= U_{\alpha}I_{\mathrm{c}}\sqrt{\frac{7}{4} - \sqrt{3}\cos\left(\theta_{\mathrm{AC}}-30^{\circ}\right)}\sqrt{1 - \left(\sin\varphi_{\mathrm{co}}\right)^{2}}.\end{aligned} \qquad (37)$$

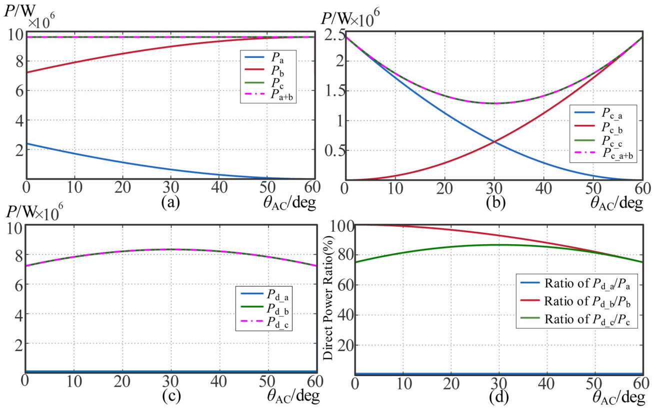

Fig. 13. Diagram of system power analysis. (a) Variation of terminal transmission power with the phase shift angle. (b) Variation of converter processing power with the phase shift angle. (c) Variation of direct transmission power with the phase shift angle. (d) Variation of the proportion of direct transmission power to terminal transmission power with the phase shift angle.

The direct transmission power can be obtained by subtracting the converter processing power from the terminal transmission power. The following (38), (39), and (40) represent the direct transmission power of the phase a, b, and c

$$P_{\mathrm{d\_a}} = P_{\mathrm{a}} - P_{\mathrm{c\_a}} \qquad (38)$$

$$P_{\mathrm{d\_b}} = P_{\mathrm{b}} - P_{\mathrm{c\_b}} \qquad (39)$$

$$P_{\mathrm{d\_c}} = P_{\mathrm{c}} - P_{\mathrm{c\_c}}. \qquad (40)$$

Additionally, the direct transmission power can also be calculated directly through the virtual midpoint potential u_{og}. For example, when analyzing the converter processing power of phase a, its complex power expression is given by

$$\begin{aligned}\dot{S}_{\mathrm{c\_a}} &= \dot{U}_{\mathrm{ao}}\dot{I}_{\mathrm{a}}^{*} = \left(\dot{U}_{\alpha} - \mathrm{j}\omega L_{\mathrm{a}}\dot{I}_{\mathrm{a}} - \dot{U}_{\mathrm{og}}\right)\dot{I}_{\mathrm{a}}^{*}\\ &= U_{\alpha}I_{\mathrm{a}}\cos\varphi_{\mathrm{a}} + \mathrm{j}\left(U_{\alpha}I_{\mathrm{a}}\sin\varphi_{\mathrm{a}} - \omega L_{\mathrm{a}}{I_{\mathrm{a}}}^{2}\right) - \dot{U}_{\mathrm{og}}\dot{I}_{\mathrm{a}}^{*}\\ &= \dot{S}_{\mathrm{a}} - \dot{U}_{\mathrm{og}}\dot{I}_{\mathrm{a}}^{*}.\end{aligned} \qquad (41)$$

In (41), the active power formed by the product of $\dot{U}_{\mathrm{og}}$ and $\dot{I}_{\mathrm{a}}$ corresponds to the direct transmission power of this port. Therefore, the selection of the reference value for the midpoint potential significantly affects the direct transmission power. Choosing the midpoint of the feeding-section voltage difference is more advantageous for enhancing the direct transmission power compared to selecting the circumcenter.

B. Theoretical Calculations Results

Using the same locomotive operating parameters as in Fig. 8, the calculation results of various power components in the system are depicted in Fig. 13.

Fig. 13(a) shows the variation of the terminal transmission power with the phase shift angle. It can be seen from Fig. 13(a) that the sum of the input powers is equal to the output power. Fig. 13(b) shows the variation of converter processing power with the phase shift angle. Fig. 13(c) shows the variation of direct transmission power with the phase shift angle. Fig. 13(d) shows the variation of the proportion of direct transmission power to terminal transmission power with the phase shift angle.

From the analysis of the results shown in Fig. 13, there is a significant difference in terminal transmission power of phase a and phase b. The significant difference in terminal transmission power is caused by the existing current control method forcing one phase current to be minimized. To address this issue, an optimized current control algorithm should be implemented to balance the currents, thereby achieving balanced terminal transmission power.

IV. CURRENT OPTIMIZATION CONTROL

A. *Principle of Current Optimization Control*

In order to solve a series of problems caused by the imbalance of input current amplitude in the solution process of Section II, the amplitude of two-phase input current should be equal in the solution process of this section. The decoupling operation should be carried out according to the coupling relationship of (1) and power balance relationship of (6) to solve the reference value of input current.

Assuming $I_a = I_b$, based on the current coupling relationship, it can be deduced that the two angles θ_A and θ_B are equal, as shown in Fig. 7(c)

$$\theta_A = \theta_B. \tag{42}$$

Consequently, (42) is substituted into the current relationship of (9), and the current relationship in (43) is obtained after simplification

$$I_a = I_b = \frac{I_c}{2\cos\theta_A} = \frac{I_c}{2\cos\theta_B}. \tag{43}$$

After substituting (7), (8), and (43) into the active power balance relationship of (6), (44) is obtained

$$\frac{U_\alpha I_c}{2\cos\theta_A}\cos(\theta_{AC}+\varphi_C-\theta_A)+\frac{U_\beta I_c}{2\cos\theta_A}\cos(\theta_{AC}+\varphi_C+\theta_B-\theta_{AB}) = U_{cg} I_c \cos\varphi_C. \tag{44}$$

Eliminating I_c at both sides of the equation and replacing θ_B with θ_A, (45) is obtained

$$\frac{U_\alpha}{2\cos\theta_A}\cos(\theta_{AC}+\varphi_C-\theta_A)+\frac{U_\beta}{2\cos\theta_A}\cos(\theta_{AC}+\varphi_C+\theta_A-\theta_{AB}) = U_{cg}\cos\varphi_C. \tag{45}$$

By separating θ_A from (44), the equation is transformed into

$$U_\alpha[\cos(\theta_{AC}+\varphi_C)+\sin(\theta_{AC}+\varphi_C)\tan\theta_A]+U_\beta[\cos(\theta_{AC}+\varphi_C-\theta_{AB})+\sin(\theta_{AC}+\varphi_C-\theta_{AB})\tan\theta_A] = 2U_{cg}\cos\varphi_C. \tag{46}$$

Upon simplification, the θ_A is obtained according to (47). Eventually, substituting θ_A into (43), I_a can be obtained

$$\tan\theta_A = \frac{2U_{cg}\cos\varphi_C - U_\alpha\cos(\theta_{AC}+\varphi_C) - U_\beta\cos(\theta_{AC}+\varphi_C-\theta_{AB})}{U_\alpha\sin(\theta_{AC}+\varphi_C) - U_\beta\sin(\theta_{AC}+\varphi_C-\theta_{AB})}. \tag{47}$$

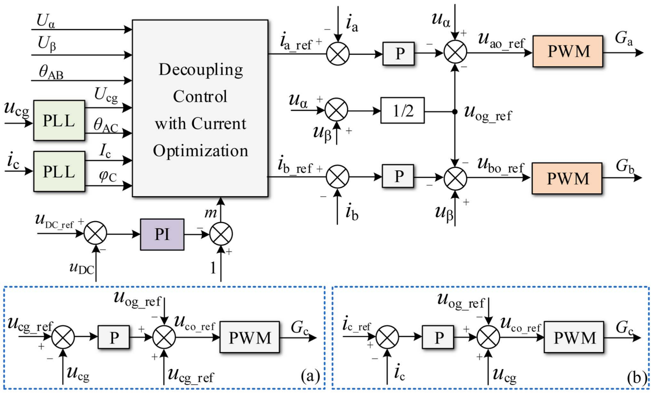

Fig. 14. Control strategy of ANSPS system. (a) Control strategy for the output bridge leg in the nontransition zone. (b) Control strategy for the output bridge leg in the transition zone.

B. *DC Voltage Control*

Due to factors such as measurement accuracy and control accuracy, it is difficult to achieve complete power balance. Additionally, sudden load changes can also cause transient fluctuations in dc voltage. To improve the correction ability of the converter's dc voltage, dc voltage control is introduced here. The key to dc voltage control resides in controlling the power difference between input power and output power. Suppose the output power is m times that of the input power with $m > 0$. Then, the expression for power relationship becomes

$$m(U_\alpha I_a\cos\varphi_A + U_\beta I_b\cos\varphi_B) = U_{cg} I_c\cos\varphi_C. \tag{48}$$

Introducing the variable m into (47), (49) can be obtained. The reference currents $\dot{I}_a$ and $\dot{I}_b$ obtained from the decoupling algorithm contain the power adjustment parameter m, thereby enabling control of the power difference between the input and the output. Under traction conditions of the locomotive, when the dc voltage exceeds the reference value, set $m > 1$ so that the input power is less than the output power. Conversely, when the dc voltage falls below the reference value, set $m < 1$ so that the input power is greater than the output power

$$\tan\theta_A = \frac{2U_{cg}\frac{\cos\varphi_C}{m} - U_\alpha\cos(\theta_{AC}+\varphi_C) - U_\beta\cos(\theta_{AC}+\varphi_C-\theta_{AB})}{U_\alpha\sin(\theta_{AC}+\varphi_C) - U_\beta\sin(\theta_{AC}+\varphi_C-\theta_{AB})}. \tag{49}$$

C. *System Control Strategy*

The control strategy of the ANSPS system is depicted in Fig. 14. The dc voltage difference passes through the PI controller. Then, subtract the output of the PI controller from 1 to get the power adjustment parameter m. Subsequently, this parameter m, combined with the measured voltage and current information, is fed into the decoupling control with current optimization to derive the reference values of a-phase and b-phase bridge leg currents. After voltage feedforward, the control signals for the corresponding input bridge legs are obtained.

There are two types of control strategies for the output bridge leg. When the train is in the nontransition zone, the control

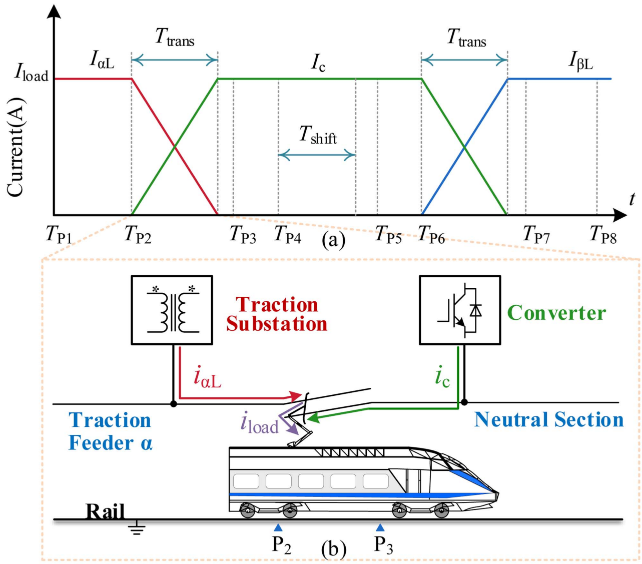

Fig. 15. Diagram of current transfer. (a) Variation of the output current reference (b) Schematic diagram of current transfer structure in the transition zone.

objective of the system is to control the neutral section voltage, enabling it to switch between the voltages of the two-phase feeding sections, and the relevant control strategy is shown in Fig. 14(a). When the train is in the transition zone, the control objective of the system is to control the output current for power transfer, and the control strategy is illustrated in Fig. 14(b).

Taking the train going from feeding section α to β as an example, the traction current of the train is denoted as $\dot{I}_{\text{load}}$. T_{P1} to T_{P8} represent the instants when the locomotive is at points P_1 to P_8 in Fig. 3, respectively. When the train arrives at point P_1, the system switches from the RPC mode to the ANSPS mode. While the train is between P_1 and P_2, the inverter side operates in no-load inversion, waiting for the train to reach P_2.

When the train is in the P_2–P_3 section, the locomotive pantograph simultaneously overlaps the neutral section and the feeding section. Consequently, the voltage of the neutral section is clamped to the voltage of feeding section α. As the train exits this overlap region (at point P_3), the pantograph disconnects from the feeding section. If there is still current flowing from the traction feeder α into the train at that moment, an instantaneous overvoltage could occur. To prevent this, it is necessary to fully transfer the locomotive's load current $\dot{I}_{\text{load}}$ from the traction feeder α to the converter before reaching point P_3. The structure during the current transfer process is shown in Fig. 15(b). The reference value for the output current $\dot{I}_{\text{c\_ref}}$ of the converter is given by

$$\dot{I}_{\text{c\_ref}} = \begin{cases} \frac{(t-T_{\text{P2}})}{T_{\text{trans}}}\dot{I}_{\text{load}} & T_{\text{P2}} \le t < T_{\text{P2}} + T_{\text{trans}} \\ \dot{I}_{\text{load}} & T_{\text{P2}} + T_{\text{trans}} \le t < T_{\text{P3}} \end{cases} \tag{50}$$

where T_{trans} denotes the current transfer time in the transition zone. Equation (50) models this process by linearly increasing the converter output current from zero to $\dot{I}_{\text{load}}$ over the total transition time T_{trans}, starting from the instant T_{P2} when the pantograph enters the transition zone at point P_2. After this time interval (i.e., when T_{P2}+$T_{\text{trans}} \le t$< T_{P3}), the reference current of converter remains constant at $\dot{I}_{\text{load}}$.

After the train reaches point P_3, the converter switches from current control to voltage control mode. The reference value of the neutral section catenary voltage is also the output voltage of the converter $u_{\text{cg·ref}}$, which is adjusted according to the position of the train

$$u_{\text{cg\_ref}} = \begin{cases} \sqrt{2}U_\alpha \sin\omega t & T_{\text{P3}} \le t < T_{\text{P4}} \\ \sqrt{2}\left(U_\alpha + \frac{t-T_{\text{P4}}}{T_{\text{shift}}} \times (U_\beta - U_\alpha)\right) & \\ \times \sin\left(\omega t + \frac{t-T_{\text{P4}}}{T_{\text{shift}}}\theta_{\text{AB}}\right) & T_{\text{P4}} \le t < T_{\text{P4}} + T_{\text{shift}} \\ \sqrt{2}U_\beta \sin\left(\omega t + \theta_{\text{AB}}\right) & T_{\text{P4}} + T_{\text{shift}} \le t < T_{\text{P6}} \end{cases} \tag{51}$$

where T_{shift} represents the time of voltage phase shift from phase α to phase β. When $T_{\text{P3}} \le t < T_{\text{P4}}$, the output voltage is maintained to match the voltage of the feeding section α.

Once the train reach point P_4, when $T_{\text{P4}} \le t < T_{\text{P4}}$+$T_{\text{shift}}$, the converter begins to perform phase-shifting control, enabling a smooth transition of neutral section voltage from the voltage of feeding section α to that of feeding section β. During this phase-shifting process, the phase angle difference between the voltages of feeding section α and feeding section β and the possible amplitude mismatch between the two traction feeder voltages must be considered. When T_{P4}+$T_{\text{shift}} \le t < T_{\text{P6}}$, the phase-shifting process will end, and the converter's output voltage will remain consistent with that of feeding section β, maintaining this state until the train enters the transition zone P_6–P_7.

Similar to the P_2–P_3 section, in the P_6–P_7 section, it is necessary to gradually transfer the load current from the converter to the traction feeder. The reference value for converter output current $\dot{I}_{\text{c\_ref}}$ is expressed as

$$\dot{I}_{\text{c\_ref}} = \begin{cases} \left(1 - \frac{(t-T_{\text{P6}})}{T_{\text{trans}}}\right)\dot{I}_{\text{load}} & T_{\text{P6}} \le t < T_{\text{P6}} + T_{\text{trans}} \\ 0 & T_{\text{P6}} + T_{\text{trans}} \le t < T_{\text{P7}} \end{cases}. \tag{52}$$

When the train is between P_7 and P_8, the converter operates in a no-load rectification state, and the inverter side operates in a no-load inverter state, waiting for the train to leave P_8. Upon the train reaching P_8, the system switches from the ANSPS mode to the RPC mode. The variation of the converter output current reference value during the train's passing through the neutral section is shown in Fig. 15(a).

D. System Power Analysis After Current Optimization

When the locomotive traction operating parameters remain identical with the load situation depicted in Fig. 8, the variation of the input current reference values after current optimization decoupling control with the phase shift angle is shown in Fig. 16. The magnitudes and phase angles of the two-phase currents are equal. During the phase shift process, the maximum current of the input bridge leg decreases from approximately 350 A to around 200 A. That is, the maximum current of the input bridge

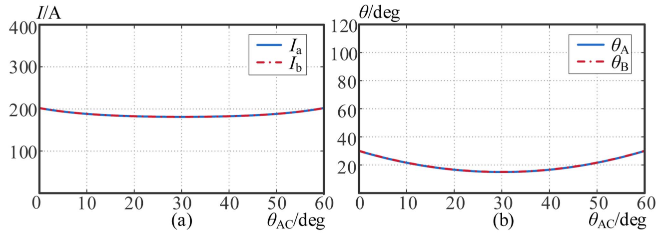

(a) (b)

Fig. 16. Reference value of input currents after current optimization. (a) Variation of current amplitude with phase shift angle. (b) Variation of current angles with phase shift angle.

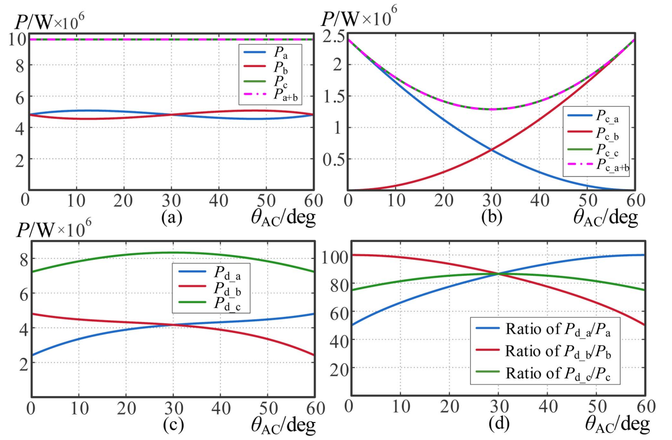

(a) (b) (c) (d)

Fig. 17. Diagram of system power analysis. (a) Variation of terminal transmission power with the phase shift angle. (b) Variation of converter processing power with the phase shift angle. (c) Variation of direct transmission power with the phase shift angle. (d) Variation of the proportion of direct transmission power in terminal transmission power with the phase shift angle.

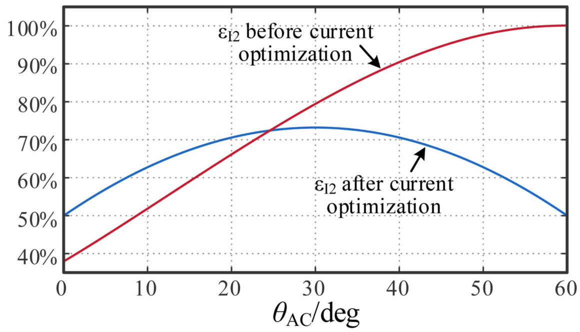

Fig. 18. Variation of current imbalance with phase shift angle.

leg decreases from the load current to 57% of its original value. Theoretically, the input bridge leg capacity required after optimization would also be significantly reduced correspondingly.

The power analysis results of the system are presented in Fig. 17. As depicted in Fig. 17(a), the input terminal transmission powers are more balanced. Fig. 17(b) indicates that the converter processing power remains unchanged compared to that before optimization. Fig. 17(c) and (d) illustrates that the total direct transmission power of the system after optimization is identical to that before optimization, while the distribution of the direct transmission power among the bridge legs is more balanced. Although the total amount of direct transmission power remains unchanged, the distribution of direct transmission power has become more reasonable through current optimization.

E. Negative Sequence Imbalance Evaluation

After conducting current optimization control, the effects on balancing the current amplitude and power become evident. In addition, this current optimization method is also beneficial for reducing the imbalance of negative sequence currents in the power grid. When the train is located in the neutral section, the currents on the low voltage side of the traction transformer are $\dot{I}_\alpha$ and $\dot{I}_\beta$, and the currents on the high voltage side are $\dot{I}_{\mathrm{A}}$, $\dot{I}_{\mathrm{B}}$, and $\dot{I}_{\mathrm{C}}$, as shown in the Fig. 3. The relationship between grid side currents and converter currents are

$$\dot{I}_{\mathrm{A}} = \frac{1}{k}\dot{I}_\alpha = \frac{1}{k}\dot{I}_{\mathrm{a}} \tag{53}$$

$$\dot{I}_{\mathrm{B}} = \frac{1}{k}\dot{I}_\beta = \frac{1}{k}\dot{I}_{\mathrm{b}} \tag{54}$$

$$\dot{I}_{\mathrm{C}} = -\left(\dot{I}_{\mathrm{A}} + \dot{I}_{\mathrm{B}}\right) = -\frac{1}{k}\left(\dot{I}_{\mathrm{a}} + \dot{I}_{\mathrm{b}}\right) \tag{55}$$

where *k* is the ratio of the traction transformer. According to the symmetrical component method, the negative sequence component and the positive sequence component of the three-phase currents in the power grid can be obtained

$$\dot{I}_{\mathrm{A}(1)} = \frac{1}{3}\left(\dot{I}_{\mathrm{A}} + a\cdot\dot{I}_{\mathrm{B}} + a^2\cdot\dot{I}_{\mathrm{C}}\right) \tag{56}$$

$$\dot{I}_{\mathrm{A}(2)} = \frac{1}{3}\left(\dot{I}_{\mathrm{A}} + a^2\cdot\dot{I}_{\mathrm{B}} + a\cdot\dot{I}_{\mathrm{C}}\right) \tag{57}$$

where $\dot{I}_{\mathrm{A}(1)}$ represents the positive sequence current component, $\dot{I}_{\mathrm{A}(2)}$ represents the negative sequence current component, and a is the operator

$$a = e^{\mathrm{j}120^\circ}. \tag{58}$$

Based on (53), (54), (55), (56), and (57), the imbalance of negative sequence current $\varepsilon_{\mathrm{I2}}$ at a measurement moment is expressed as

$$\varepsilon_{\mathrm{I2}} = \left|\frac{\dot{I}_{\mathrm{A}(2)}}{\dot{I}_{\mathrm{A}(1)}}\right| \times 100\% = \left|\frac{(1-a)\,\dot{I}_{\mathrm{a}} + \left(a^2-a\right)\cdot\dot{I}_{\mathrm{b}}}{\left(1-a^2\right)\dot{I}_{\mathrm{a}} + \left(a-a^2\right)\cdot\dot{I}_{\mathrm{b}}}\right| \times 100\%. \tag{59}$$

The variation of negative sequence current imbalance in the process of voltage phase shift in the neutral section is shown in Fig. 18. Before the current control optimization, the negative sequence current imbalance becomes more significant when the phase shift angle exceeds 30°.

In order to better evaluate the imbalance of negative sequence current, the root mean square value is commonly used to represent the imbalance over a period of time. During this period, the imbalance of negative sequence current is denoted as ε. A total of *y* points are sampled, and the imbalance degree of the

TABLE II
MAIN PARAMETERS

Parameters	Values	Parameters	Values
U_α(kV)	27.5	L_a(mH)	10
U_β(kV)	27.5	L_b(mH)	10
θ_{AB}(deg)	60	L_c(mH)	10
U_{dc} (kV)	45	DC Capacitor (mF)	5
Rated Power(kW)	9600	Simulation Step Size (s)	1×10^{-6}

TABLE III
TIME SEQUENCE PARAMETERS OF ANSPS

Positions	Time(s)	Positions	Time(s)
P_1	0.0	P_2	0.3
P_3	0.6	P_4	1.0
P_5	2.0	P_6	2.4
P_7	2.7	P_8	3.0
T_{shift}	1	T_{trans}	0.3

nth point is denoted as $\varepsilon_{I2(n)}$

$$\varepsilon = \sqrt{\frac{1}{y}\sum\nolimits_{n=1}^{y} \varepsilon^2_{I2(n)}}. \tag{60}$$

The imbalance of negative sequence current ε before current control optimization is 78.3% . After the current control optimization, the negative sequence current imbalance ε is 65.7% . After the current control optimization, the imbalance of negative sequence current is significantly reduced.

V. SIMULATION RESULTS

In this section, the feasibility of the current decoupling optimization control proposed in this article is verified based on the MATLAB/Simulink, and its optimization effect is discussed. The main parameters of the circuit are shown in Table II. The simulation process corresponds to the train travelling process shown in Fig. 3, the time T_{trans} of transition zone is 0.3 s, and the phase shifting time T_{shift} is 1 s. The time sequence parameters are shown in Table III.

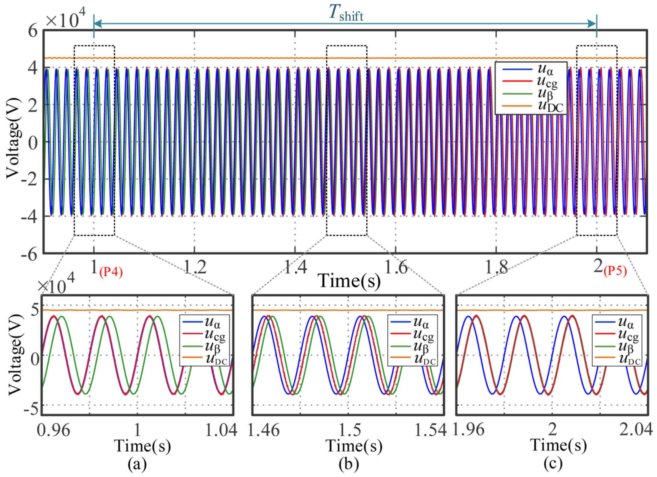

Fig. 19. Simulation waveform of output voltages and DC voltage. (a) Simulation waveform before the phase shifting. (b) Simulation waveform when the phase shift angle of the neutral section voltage is 30°. (c) Simulation waveform after the phase shifting.

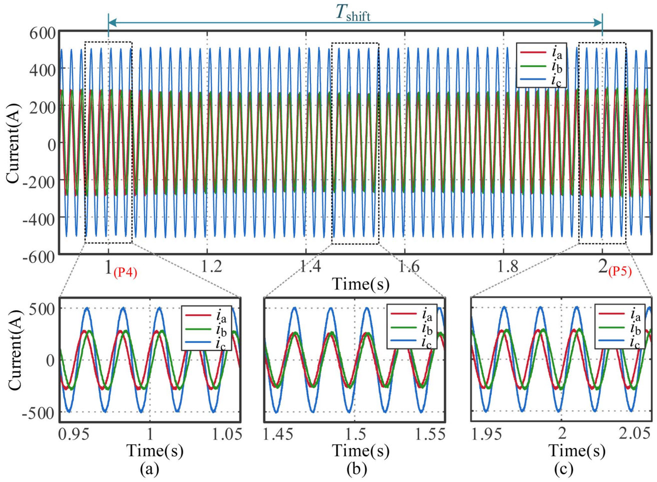

Fig. 20. Simulation waveform of phase currents. (a) Simulation waveform before the phase shift. (b) Simulation waveform when neutral section voltage at phase shift of 30°. (c) Simulation waveform after the phase shift.

Taking the train passing through the neutral section from left to right as an example, as shown in Fig. 3, from P_1 point to P_8 point in turn. The output voltage and dc voltage simulation waveforms are shown in Fig. 19. The voltage phase of neutral section starts to shift from the feeding section α to the feeding section β at 1 s, and the phase shift process is completed at 2 s. Fig. 19(a) shows the simulation waveform of the neutral section voltage u_{cg} before the phase shifting, and the phase of neutral section voltage u_{cg} is consistent with that of feeding section α. Fig. 19(b) shows the waveform in the phase shifting process, and u_{cg} is located between the voltage of two feeding sections. Fig. 19(c) shows the simulation waveform after phase shifting, where the neutral section voltage u_{cg} coincides with the voltage of feeding section β. In this process, the dc voltage is kept constant and the voltage ripple is small.

Fig. 20 illustrates the variation of current during the process shown in Fig. 19. Despite the increase in the phase shift angle, the currents of the two-phase bridge legs at the input remain equal, which demonstrates the effectiveness of the current decoupling optimization control.

Fig. 21 presents the current situation within the transition zones. Specifically, within the time intervals of 0.3–0.6 s and 2.4–2.7 s, it is in the left transition zone P_2–P_3 and the right transition zone P_6–P_7, respectively. During the period of 0.3–0.6 s, the load current gradually transfers from the current $i_{\alpha L}$ of the α-phase feeding section to the output current i_c of the converter. In the right transition zone, the load current gradually transfers from the converter to the current $i_{\beta L}$ of the β-phase feeding section. It can be observed from Fig. 21(a) and (b) that the current amplitudes of the input bridge legs are always equal

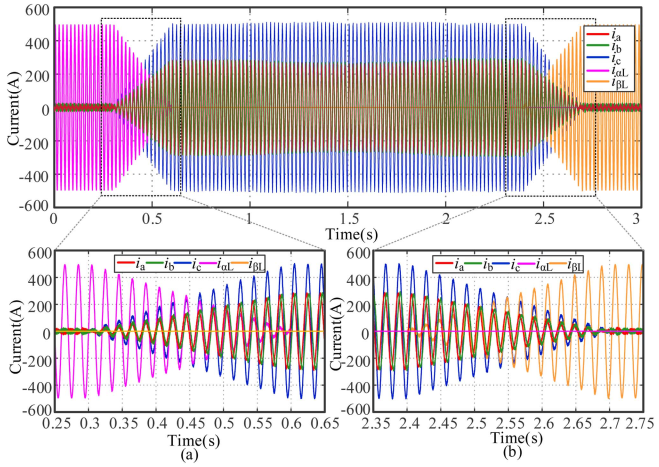

Fig. 21. Simulation waveform of phase currents within the transition zone. (a) Waveform of phase currents within transition zone where the train is about to enter the neutral section. (b) Waveform of phase currents within transition zone where the train is about to leave the neutral section.

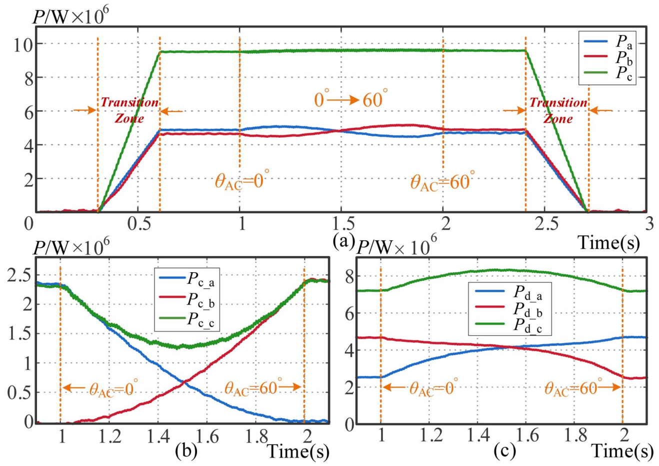

Fig. 22. Simulation waveform of power. (a) Simulation waveform of terminal transmission power. (b) Simulation waveform of converter processing power. (c) Simulation waveform of direct transmission power.

even within the transition zones. The results shown in Figs. 20 and 21 demonstrate that the current decoupling optimization control can effectively balance the current amplitudes on the input side.

Since the phase shifting of the output voltage is gradual and slow, the power analysis during the phase shifting process can be approximately equivalent to a steady-state process. Based on the power calculation methods for terminal transmission power, converter processing power and direct transmission power in Section III, the corresponding values are calculated using simulation data. The results are shown in Fig. 22. Fig. 22(a) illustrates the time-domain variation of terminal transmission power throughout the entire process of the train passing through the neutral section. The correlation between time and train position is described in Table III. At t = 0.3 s, the train enters the transition zone, initiating the current transfer control process. Correspondingly, the output power of the converter begins to gradually increase, indicating that the traction power of the locomotive is progressively transferred from the traction feeder to the converter of the ANSPS system. During this transition period, the terminal transmission power at the two input phases also increases gradually and remains evenly distributed. At t = 1 s, the phase-shifting control of the output voltage is applied. During this process, the terminal transmission power remains relatively balanced, and its variation closely matches the theoretical trends shown in Fig. 17(a). Fig. 22(b) shows the simulated waveform of the converter processing power, while Fig. 22(c) presents the simulated waveform of the direct transmission power. Both waveforms are consistent with the theoretical power curves shown in Fig. 17(b) and (c), respectively.

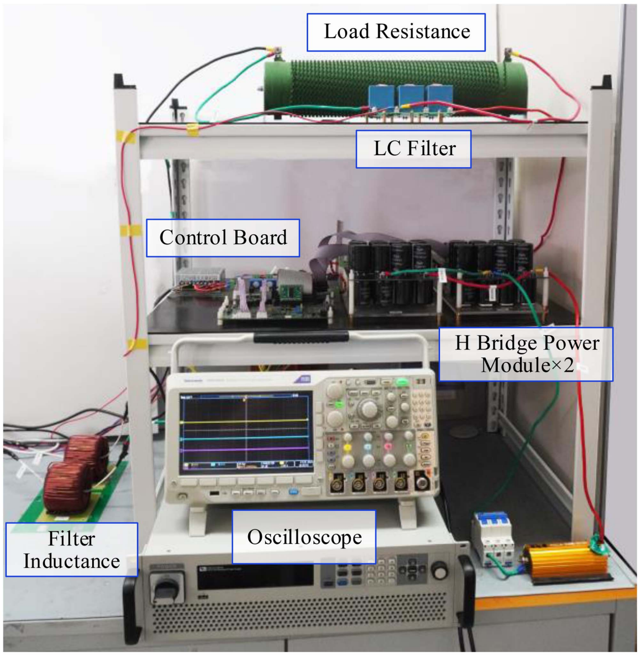

Fig. 23. Photo of scaled-down experimental prototype.

The consistency between the simulated waveforms and the theoretical curves validates the correctness of the power calculation methods proposed in Section III. Furthermore, the balance in terminal transmission power distribution confirms the effectiveness of the proposed current optimization control.

VI. EXPERIMENTAL RESULTS

In order to further verify the effectiveness and the superiority of the control strategies proposed in this article, a corresponding scaled-down experimental prototype is built, as shown in Fig. 23. Its main parameters are shown in Table IV.

The three-phase power grid supplies power to the experimental prototype via a three-phase autotransformer-based voltage regulator. Two line voltages from the voltage regulator output are employed to emulate the traction feeder voltage. In the traction feeders, the rms value of the voltage is 220 V, and the phase-α voltage leads the phase-β voltage by 60°. The main power circuit consists of a three-phase converter constructed with two full-bridge power modules, one of which uses only

TABLE IV
MAIN PARAMETERS OF EXPERIMENTAL PROTOTYPE

Parameters	Values	Parameters	Values
Voltage of traction feeder α	220 V	Phase of traction feeder α	0°
Voltage of traction feeder β	220 V	Phase of traction feeder β	-60°
Voltage of neutral section	220 V	Dc voltage	400 V
Branch inductor	5 mH	Capacitor in dc side	4.84 mF
Load resistance	25 Ω	Switching frequency	10 kHz

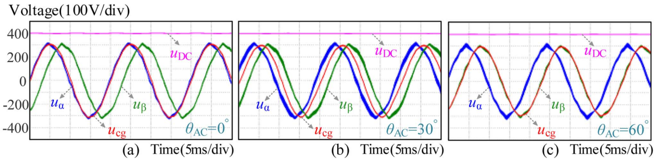

Fig. 24. Voltage waveforms in the experiment. (a) Neutral section voltage before the phase shifting ($\theta_{AC} = 0°$). (b) Neutral section voltage when the phase shift angle is 30° ($\theta_{AC} = 30°$). (c) Neutral section voltage after the phase shifting ($\theta_{AC} = 60°$).

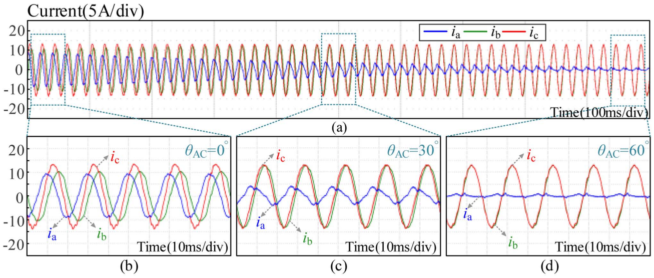

Fig. 25. Current waveforms without using the current optimization control in the experiment. (a) Phase currents in the whole process. (b) Phase currents before the phase shifting ($\theta_{AC} = 0°$). (c) Phase currents when the phase shift angle is 30° ($\theta_{AC} = 30°$). (d) Phase currents after the phase shifting ($\theta_{AC} = 60°$).

one leg. Both the switching frequency and the control frequency are set at 10 kHz. When the neutral section voltage is switched from the traction feeder α to the traction feeder β, the voltage waveform of the experiment is shown in Fig. 24.

Fig. 24(a) shows the voltage waveforms before the phase shifting. The neutral section voltage before the phase shifting is consistent with the voltage of traction feeder α. Fig. 24(b) shows the voltage waveform when phase shift angle θ_{AC} is about 30°, with the neutral section voltage between the voltages of feeding section α and feeding section β. Fig. 24(c) shows the voltage waveforms after the phase shifting. The neutral section voltage after the phase shifting is consistent with the voltage of traction feeder β. The experimental results show that the neutral section voltage can be smoothly transitioned, with the dc voltage remaining at 400 V during this period.

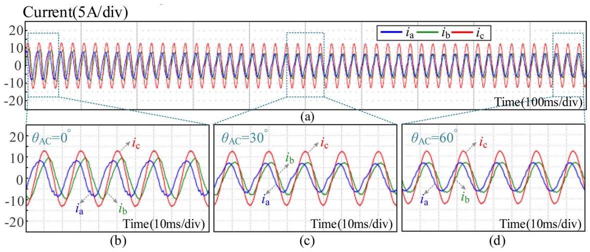

Fig. 26. Current waveforms using the current optimization control in the experiment. (a) Phase currents in the whole process. (b) Phase currents before the phase shifting ($\theta_{AC} = 0°$). (c) Phase currents when the phase shift angle is 30° ($\theta_{AC} = 30°$). (d) Phase currents after the phase shifting ($\theta_{AC} = 60°$).

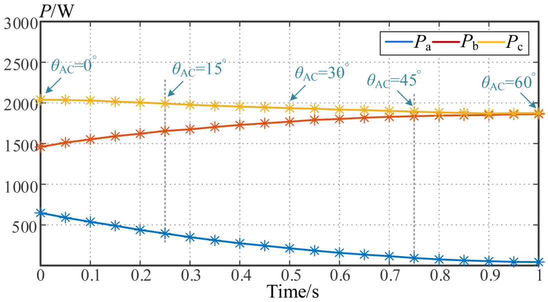

Fig. 27. Terminal transmission power waveforms without using the current optimization control in the experiment.

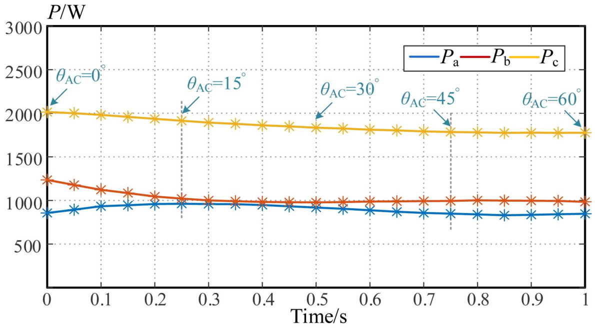

Fig. 28. Terminal transmission power waveforms using the current optimization control in the experiment.

The current experimental waveform without current optimization control is shown in Fig. 25. It can be seen from the Fig. 25 that the amplitude difference between the a-phase leg current i_a and the b-phase leg current i_b is relatively large, especially when the phase shift angle is 60°. The difference is more obvious.

The current experimental waveform after using current optimization control is shown in Fig. 26. Fig. 26(a) shows the waveform of each phase current in the whole phase shift process. The amplitude of i_a and i_b is basically the same. Fig. 26(b), (c), and (d) shows the current experimental waveforms when the phase shift angles are 0, 30, and 60 degrees, respectively. It can be seen from them that the input currents i_a and i_b can still be balanced under these phase shift angles, and the maximum value of the input currents during the phase shift process is also reduced. The current optimization control effect meets expectations.

In the experiment, when the phase shift angle changes by three degrees, the voltage and current of one cycle are selected to calculate the power at this point. The power calculation results without current optimization control are shown in Fig. 27, and the power calculation results using current optimization control are shown in Fig. 28. It can be seen from the Fig. 27 that the transmission power of the terminal transmission power of phase b is higher than that of phase a, and the power imbalance is obvious. After applying the current optimization control, as shown in Fig. 28, and the distribution of transmission power between phase a and phase b is more average, which also verifies the effectiveness of the current optimization control.

VII. CONCLUSION

This article begins with an analysis of the circuit characteristics of the ANSPS system to explore its coupling mechanism. The basic principle of the existing current decoupling control is analyzed, and its drawbacks, including a significant difference in current amplitude and uneven power distribution, are pointed out. Subsequently, the terminal transmission power, converter processing power and direct transmission power are calculated, while the transmission path and the proportion of the direct transmission power are analyzed. Through these efforts, a clearer understanding of the power flow within the system has been achieved. Then, a new current optimization control method is put forward. Based on ensuring continuous power supply in the neutral section without overvoltage and arcs, this method enables the current amplitudes of the input legs to remain equal throughout the process of the train passing through the neutral section, which is beneficial to converter design. During the entire process of voltage phase shift in the neutral section, the maximum current amplitude of the input legs can be reduced, and the converter capacity of the input legs can be further decreased theoretically. Additionally, the terminal transmission power becomes more balanced, and the negative sequence unbalance degree on the grid side is also lowered. In conclusion, the power analysis conducted in this article and the proposed current optimization control method have a significantly positive impact on the design of the converter.

REFERENCES

[1] M. Brenna, F. Foiadelli, and H. J. Kaleybar, "The evolution of railway power supply systems toward smart microgrids: The concept of the energy hub and integration of distributed energy resources," *IEEE Electrific. Mag.*, vol. 8, no. 1, pp. 12–23, Mar. 2020.

[2] S. M. M. Gazafrudi, A. T. Langerudy, E. F. Fuchs, and K. Al-Haddad, "Power quality issues in railway electrification: A comprehensive perspective," *IEEE Trans. Ind. Electron.*, vol. 62, no. 5, pp. 3081–3090, May 2015.

[3] Y. Ge, H. Hu, Y. Huang, J. C. K. Wang, and Z. He, "Quadratic sensitivity models for flexible power quality improvement in ac electrified railways," *IEEE Trans. Power Electron.*, vol. 38, no. 3, pp. 2844–2849, Mar. 2023.

[4] H. Hu et al., "Traction power systems for electrified railways: Evolution, state of the art, and future trends," *Railway Eng. Sci.*, vol. 32, no. 1, pp. 1–19, Mar. 2023.

[5] J. Y. Chen et al., "Power flow control-based regenerative braking energy utilization in ac electrified railways: Review and future trends," *IEEE Trans. Intell. Transp. Syst.*, vol. 25, no. 7, pp. 6345–6365, Jul. 2024.

[6] Z. Zhang, T. Q. Zheng, Z. Zhang, K. Li, and S. Yang, "A modified thyristor-based auto-passing neutral section scheme with one auxiliary transformer," *IEEE Access*, vol. 12, pp. 122795–122804, Jul. 2024.

[7] Z. Zhang, Z. Zhang, K. Li, R. Hao, X. You, and T. Q. Zheng, "An uninterruptible smart electric neutral section executer for AC electrified railway," in *Proc. IEEE 12th Energy Convers. Congr. Expo. - Asia*, 2021, pp. 2040–2045.

[8] K. Huang, G. B. Lin, Z. Liu, and Y. Yang, "Research on transient overvoltages of high-speed train passing articulated split-section insulator," *IEEE Trans. Transp. Electrific.*, vol. 9, no. 1, pp. 1664–1682, Mar. 2023.

[9] Z. Li et al., "Active disturbance rejection control for static power converters in flexible ac traction power supply systems," *IEEE Trans. Energy Convers.*, vol. 37, no. 4, pp. 2851–2862, Dec. 2022.

[10] Z. Li, X. Li, Y. Wei, C. Lu, Y. Lin, and Z. Li, "Ground fault analysis and grounding method of static power converters in flexible AC traction power supply systems," *IEEE Trans. Power Electron.*, vol. 37, no. 5, pp. 5535–5546, May 2022.

[11] X. He et al., "Advanced co-phase traction power supply system based on three-phase to single-phase converter," *IEEE Trans. Power Electron.*, vol. 29, no. 10, pp. 5323–5333, Oct. 2014.

[12] M. Lei, Y. Wang, and C. Zhao, "Optimized operation of the full-bridge five-branch modular multilevel converter for power quality enhancement of co-phase railway power system," *IEEE Trans. Transp. Electrific.*, vol. 8, no. 1, pp. 590–604, Mar. 2022.

[13] Z. Zhang et al., "Smart electric neutral section executer embedded with automatic pantograph location technique based on voltage and current signals," *IEEE Trans. Transp. Electrific.*, vol. 6, no. 3, pp. 1355–1367, Sep. 2020.

[14] Z. Zhang, K. Li, Z. Zhang, T. Q. Zheng, R. Hao, and X. You, "A thyristor-based auto-passing neutral section scheme with auxiliary transformers for AC electrified railway," *IEEE Trans. Transp. Electrific.*, vol. 9, no. 2, pp. 2296–2307, Jun. 2023.

[15] H. Hayashiya et al., "Investigation of closing surge in shinkansen power system and proposal of a novel power electronics application for changeover section," *IEEJ Trans. Ind. Appl.*, vol. 126, no. 7, pp. 857–864, 2006.

[16] Z. Ni, F. Xiao, J. Yuan, and Y. Ke, "Research on uninterrupted phase-separation passing device based on three-phase MMC," in *Proc. IEEE PES Asia-Pacific Power Energy Eng. Conf.*, 2019, pp. 1–6.

[17] X. Tian, Q. Jiang, and Y. Wei, "Two-phase modular multilevel converter topology study of railway uninterruptible phase-separation passing device," *Power Syst. Technol.*, vol. 39, no. 10, pp. 2901–2906, Oct. 2015.

[18] X. Tian, Q. Jiang, and Y. Wei, "Research on novel uninterruptible phase-separation passing scheme in electrified railways," *Power Syst. Protection Control*, vol. 40, no. 21, pp. 14–18, Nov. 2012.

[19] S. Cheng et al., "Structure improvement and control algorithm optimization-based ground automatic neutral-section passing method for train," *IEEE J. Emerg. Sel. Topics Power Electron.*, vol. 11, no. 3, pp. 2879–2894, Jun. 2023.

[20] Z. Ni et al., "Multi-function uninterrupted phase-separation passing system and its control method," *CSEE J. Power Energy Syst.*, vol. 9, no. 6, pp. 2332–2343, Nov. 2023.

[21] X. Tian, Q. Jiang, and Y. Wei, "Research on novel railway uninterruptible flexible connector with series-connected transformers and back-to-back converter," in *Proc. IEEE ECCE Asia Downunder*, 2013, pp. 111–116.

[22] Y. Huang, H. Hu, Y. Wang, Y. Ge, and Y. Gu, "Flexible uninterrupted phase-separation passing system and its control strategy for electrified railway trains," *Trans. China Electrotechnical Soc.*, vol. 36, no. 23, pp. 4959–4969, Dec. 2021.

[23] Y. Ge, Y. Huang, J. Chen, K. Wang, H. Hu, and Z. He, "Wide-adaptable uninterrupted power supply system for neutral sections of ERs with event-triggered flexible power and voltage control," *IEEE Trans. Power Electron.*, vol. 39, no. 12, pp. 16566–16579, Dec. 2024.

[24] W. Wang, Z. Li, C. Zhao, Y. Hu, and Y. Li, "Research on partial capacity phase-separation passing equipment control strategy," *Proc. CSEE*, vol. 39, no. 5, pp. 1461–1470, Mar. 2019.

[25] Z. Zhang, T. Q. Zheng, C. Gao, K. Li, and J. Guo, "An automatic neutral section power supplier serving as railway power conditioner on time-division basis," *IEEE Trans. Power Electron.*, vol. 39, no. 8, pp. 9329–9343, Aug. 2024.

[26] K. Li et al., "Analysis and correction of a pantograph location method based on current information of traction network," *IEEE Trans. Transp. Electrific.*, vol. 7, no. 3, pp. 1858–1869, Sep. 2021.

[27] H.-J. Lee, S. W. Yoon, and Y.-D. Yoon, "Hybrid distribution transformer based on an existing distribution transformer and a series-connected power converter," *IEEE Trans. Power Del.*, vol. 37, no. 5, pp. 4202–4211, Oct. 2022.

[28] C. Li and J. A. Cobos, "Classification of differential power processing architectures based on VA area modeling," *IEEE J. Emerg. Sel. Topics Power Electron.*, vol. 10, no. 6, pp. 7849–7866, Dec. 2022.

Zhibo Zhang (Graduate Student Member, IEEE) was born in Tieling, China, in 1996. He received the B.S. degree in electrical engineering in 2019 from Beijing Jiaotong University, Beijing, China, where he is currently working toward the Ph.D. degree in power electronics with the School of Electrical Engineering.

His current research interests include railway electrification system, partial power processing converter, and modular multilevel converter.

Kai Li (Senior Member, IEEE) received the B.S. degree in electrical engineering from Wuhan University, Wuhan, China, in 2011, and the Ph.D. degree in electrical engineering from Tsinghua University, Beijing, China, in 2017.

He was a Visiting Scholar with the Center for Power Electronics Systems, Virginia Tech, Blacksburg, VA, USA, from 2013 to 2015. He was a Postdoctoral Fellow with Tsinghua University, from 2017 to 2019. In 2019, he was with the School of Electrical Engineering, Beijing Jiaotong University, Beijing, China, where he is currently an Associated Professor. His current research interests include solid-state transformer, railway electrification system, modular multilevel converters, and electrolytic hydrogen production converters.

Changyu Gao (Graduate Student Member, IEEE) was born in Jinan, China, in 1997. He received the B.S. degree in electrical engineering from Shandong University of Science and Technology, Qingdao, China, in 2019. He is currently working toward the Ph.D. degree in electrical engineering with Beijing Jiaotong University, Beijing, China.

His current research interests include multiport dc–dc converters and solid-state-transformers.

Trillion Q. Zheng (Senior Member, IEEE) received the B.S. degree from Southwest Jiaotong University, Sichuan, China, in 1986, and the M.S. and Ph.D. degrees from Beijing Jiaotong University, Beijing, China, in 1992 and 2002, respectively, all in electrical engineering.

He is currently a University Distinguished Professor with Beijing Jiaotong University. He is also the Director with the Center for Electric Traction, Beijing Jiaotong University, founded by Ministry of Education, China. His current research interests include the power supplies and ac drives of railway traction systems, high-performance and low-loss power electronics systems, PV-based converters and control, active power filters, and power quality correction.

Dr. Zheng was the recipient of the Youth Award of Railway Science and Technology of Zhan Tianyou in 2005 and the Zhongda Scholar for power electronics and motor drive area by the Delta Environmental and Educational Foundation in 2007.